JP1J.7

PROGRESS IN DOPPLER RADAR DATA ASSIMILATION

Qin Xu*, National Severe Storms Laboratory, Norman, OK
Kang Nai, Li Wei, Pengfei Zhang, Leilei Wang, and Huijuan Lu, CIMMS, University of Oklahoma, Norman, OK
Qingyun Zhao, Naval Research Laboratory, Monterey, CA

1. Introduction

A phased array weather radar has been constructed at NSSL Norman Oklahoma, and this establishes the first National Weather Radar Testbed equipped with the state-of-the-art (solid-state) phased-array antenna (Forsyth et al. 2005). An important and yet very challenging research goal is to optimally design and utilize the electronically-controlled agile beam scans for various meteorological applications. This includes assimilating phased array radar observations into mesoscale models to improve numerical analyses and predictions of severe storms and other hazardous weather conditions. This paper reports our research progress in this direction.

2. Radar data and background fields

The phased array radar radial-velocity and reflectivity data used in this study were collected during the period from 2100 to 2200 UTC when a four-quadrant electronic-scan strategy was tested on 2 June 2004. During this period, a squall line moved southeastward through the central Oklahoma area in the radial range (140 km) of the phased array radar scans (Fig. 1). The radar scanned roughly every two minutes per volume. Total 26 volume scans were collected. Among these 26 volume scans, there is one volume scan that covers only a single quadrant and this volume is not used. The remaining 25 volume scans cover all the four quadrants and are used in this study. Each volume scan has 7 tilts with elevation angles of 0.75, 2.27, 3.78, 5.28, 6.78, 8.28 and 9.28 degree. On each tilt, the spatial resolutions are 240 m in the radial direction and approximately 1.5^{o} in the azimuthal direction.

The Coupled Ocean/Atmosphere Mesoscale Prediction System (COAMPS, Hodur 1997) is used to produce the background fields. The model is configured with three nested domains centered over the state of Oklahoma with resolutions of 54, 18 and 6 km for the coarse, medium and fine grids, respectively, and 30 levels in the vertical. All other parameters are set to be the same as COAMPS operational runs. The model (control run) is initialized (cold start) at 0000 UTC 2 June 2004. After the first 12-hr model run, the conventional observations are assimilated, and then another 12-hr run is launched (warm start). The predicted wind fields on the 6 km grid are used for radar radial-velocity dealiasing in section 3, for error covariance estimation in section 4, and for radar data assimilation in section 5.

3. Phased array radar data quality control

The radar data quality control checks and corrects velocity alias errors caused by the finite range of radar velocity measurements limited by the Nyquest velocity. Since the COAMPS background velocity is used as the reference field, the dealiasing technique used here is a simplification of the three-step dealiasing of Gong et al. (2003, referred to as GWX). It performs only two steps: reference check and continuity check. The reference check is similar to that used in the first two steps of the three-step dealiasing of GWX except that the reference velocities are provided by COAMPS predictions instead of the modified VAD and classic VAD. The continuity check (buddy check) is similar to the third step described in section 2d of GWX. For the phased array radar velocity data used in this study, this simplified two-step dealiasing is found to be effective (as shown Fig. 1) and better than the operationally used technique.

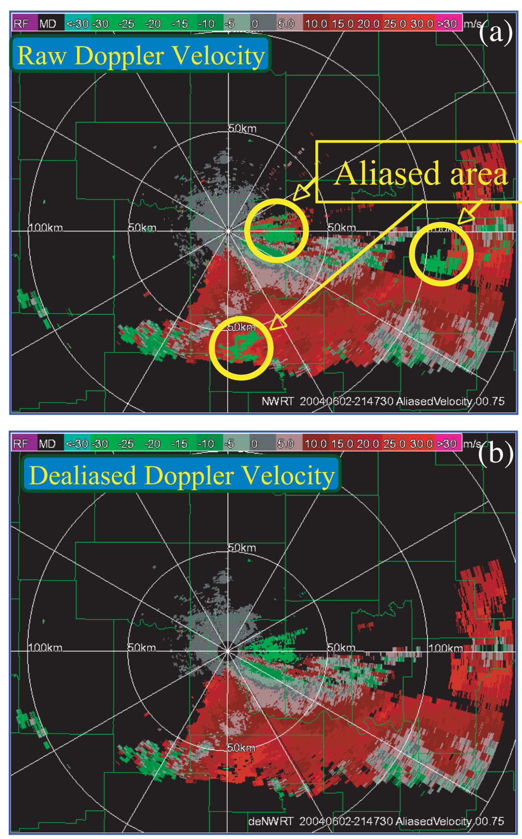

Fig. 1. Phased array radar observed radial velocity (a) and dealieased radial velocity (b) at 21:47 UTC on 2 June 2004. The aliased velocity areas are highlighted by yellow circles in (a).

* *Corresponding author address:* Qin Xu, NSSL, 1313 Halley Circle, Norman, OK 73069;
e-mail: Qin.Xu@nssl.noaa.gov.

After the dealiasing, an additional step of data quality control is performed to remove outliers. A radial-velocity measurement is considered to be an outlier if the absolute value of its difference from the radial-velocity averaged over its neighboring nine gates along the radar beam is more than 1.25 times as large as the nine-point radial-velocity standard deviation. Detected and removed outliers are about 10% of the total amount of the phased array velocity data, and the phased array radar velocity data appear to be noisier than the WSR-88D velocity measurements from the Oklahoma City KTLX radar for the same squall line on 2 June 2004. Finally, the precipitation terminal velocity is estimated from radar observed reflectivity (Kessler 1969) and its projection on the radar beam is removed from the radar observed radial velocity.

4. Error covariance estimation

The background horizontal wind error is considered as a random vector field. This random vector field is assumed to be statistically homogeneous and isotropic in the horizontal. The covariance of the radial-component field of this random vector field has the following non-isotropic form on the conic surface of low-tilt radar scans (Xu and Gong 2003, referred to as XG):

$$C_{vr}(\mathbf{x}_i, \mathbf{x}_j) = [C_+(r)\cos\beta_- + C_-(r)\cos\beta_+]/2, \qquad (1)$$

where $\mathbf{x}_i = (x_i, y_i)$ denotes the location of the i-th point relative to the radar (at the origin of the coordinates), $C_+(r) = C_{ll}(r) + C_{tt}(r)$, $C_-(r) = C_{ll}(r) - C_{tt}(r)$, $\beta_- = \Delta\beta_i - \Delta\beta_j$ and $\beta_+ = \Delta\beta_i + \Delta\beta_j$. Here, $C_{ll}(r)$ and $C_{tt}(r)$ are the two diagonal terms in the canonical form of the vector wind error covariance tensor [see (2.1)-(2.2) of XG], while $\Delta\beta_i$ and $\Delta\beta_j$ are the angles that rotate vector $\mathbf{x}_j - \mathbf{x}_i$ to the directions of vectors $\mathbf{x}_i$ and $\mathbf{x}_j$, respectively, measured positive counterclockwise (see Fig. 1 of XG). Note that $C_{ll}(r)$ and $C_{tt}(r)$ are functions of $r = |\mathbf{x}_i - \mathbf{x}_j|$ only and their function forms need to be estimated.

The non-isotropic error covariance function in (1) suggests that the conventional statistic method of innovation analysis (Xu and Wei 2001, referred to as XW) can be modified to utilize radar wind innovation (observation minus background) data. Based on (1), the covariance of normalized radial-velocity innovation data can be partitioned as follows:

$$\langle d_i d_j \rangle = \begin{cases} \sigma_d^{-2} C_{vr} & \text{for } r \geq r_o \\ \sigma_d^{-2}(C_{vr} + C_{vr}^{ob}) & \text{for } r < r_o\,, \end{cases} \qquad (2)$$

where <( )> denotes the ensemble mean of ( ), $d_i = v_{rdi}/\sigma_{di}$, $\sigma_{di} = \langle (v_{rdi})^2 \rangle^{1/2}$, v_{rdi} is the radial-velocity innovation at the i-th observation point, σ_d^2 is the averaged value of $(\sigma_{di})^2$ over all (qualified) observation points, C_{vr}^{ob} is the radar radial-velocity observation error covariance, and r_o is the range of observation error correlation. The true mean of d_i is assumed to be negligibly small in (2) although the computed $\langle d_i \rangle$ may not be small. The ensemble mean on the left-hand side of (2) can be computed from the sampled time series of $d_i d_j$ for each (i, j) pair of observation points. The background error covariance C_{vr} is modeled by (1) with $C_+(r)$ and $C_-(r)$ expressed by the truncated spectral expansions in (4.1) of XW, but the range of background error correlation is now set to D = 160 km based on the overall distribution of the computed innovation covariances. The range of observation error correlation is set to r_o = 2 km based on the computed innovation covariance structure near r = 0. Within the range of $0 \leq r \leq r_o$, there are too few data points to resolve the structure of C_{vr}^{ob}, so only the variance $\sigma_{ob}^2 = C_{vr}^{ob}|_{r=0}$ is estimated. The partition in (2) is similar to that in Xu et al. (2003, XWN), but the innovation data are normalized to improve their statistical homogeneity. By subtracting their respective background fields (provided by the COAMPS predictions as described in section 2) from the 25 fields of quality-controlled radial-velocity observations at the lowest tilt (0.75^o), 25 innovation fields are generated and used to compute $\langle d_i d_j \rangle$ in (2).

Ideally, the normalized innovation covariance on the right-hand side of (2) should be computed for each qualified pair of observation points (for which the sampled time series $d_i d_j$ cover no less than 60% of the total 25 time levels). This, however, will take too much computer time to allow the intended real-time application. (Note that there are often more than 10^5 observation points and thus more than 0.5×10^{10} pairs on the lowest tilt of radar scans). To solve this problem, the innovation covariances are computed in this paper not for all the qualified pairs (as in XWN) but for thinned qualified pairs. The thinned pairs are those on the same beams, two opposite beams, and on each of the five selected circles (with r = 14.4, 19.2, 24.0, 28.8, and 33.6 km).

For pairs of observation points on the same beam (or two opposite beams), we have $\cos\beta_- = 1$ and $\cos\beta_+ = 1$ (or $\cos\beta_- = -1$ and $\cos\beta_+ = -1$) and thus $C_{vr} = C_{ll}(r)$ [or $C_{vr} = -C_{ll}(r)$] in (1). In this case, the normalized innovation covariances are binned every 240 m in r along each beam for all the beams with $\cos\beta_-$ and $\cos\beta_+$ fixed. The binned innovation covariances are plotted in Fig. 2a. For pairs on each selected circle, the normalized innovation covariances are binned every beam width (about 1.5^o in the azimuth). In this case, r, β_-, β_+ and thus C_{vr} in (1) are functions of the azimuthal separation between points $\mathbf{x}_1$ and $\mathbf{x}_2$ along the selected circle. Thus, C_{vr} can be also viewed as a function of r along the selected circle, as shown by the two curves fitted to their respective binned innovation covariances in Fig.

2b along the first two circles (with r = 14.4 and 19.2 km).

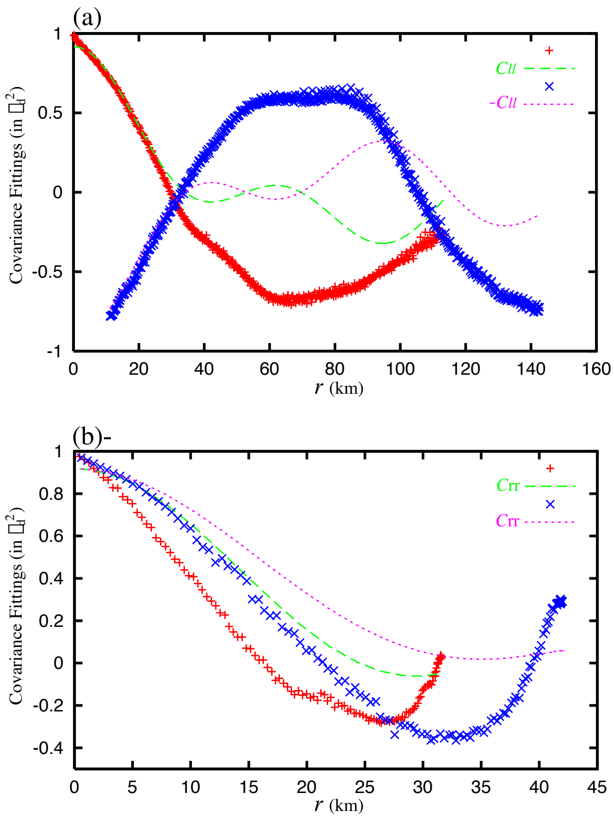

Fig. 2. Binned innovation covariances (normalized by σ_d^2 = 76.8 m^2 s^{-2}) for qualified pairs on the same beams [marked by + signs in (a)], on two opposite beams [marked by x signs in (a)], on the first selected circle with r = 14.4 km [marked by + signs in (b)], and the second selected circle with r = 24.0 km [marked by x signs in (b)]. In each panel, the green (or purple) curve is the estimated background error covariance function that fits the + signs (or x signs).

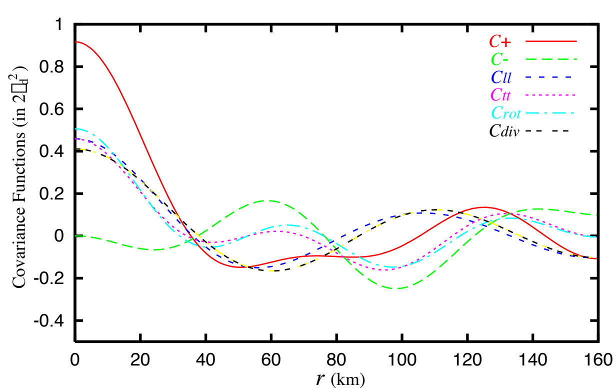

Fig. 3. Estimated background error covariance functions scaled by $2\sigma_d^2$ (= 76.8 m^2 s^{-2}).

The estimated background error covariance functions are scaled by $2\sigma_d^2$ and plotted in Fig. 3. Note that $C_+(0) = 2\sigma^2$ is the background vector wind error variance, so σ^2 is the error variance for each component (such as the radial component) of the background vector wind. The vertical interception of $0.5\sigma_d^{-2}C_+(r)$ at $r = 0$ in Fig. 3 estimates σ^2/σ_d^2 = 0.9. The innovation variance is σ_d^2 = 76.8 m^2 s^{-2} (not shown) which is the sum of σ^2 and σ_{ob}^2. This gives σ^2 = 70.4 m^2 s^{-2} and σ_{ob}^2 = 6.4 m^{2}s^{-2} or, equivalently, σ = 8.4 m s^{-1} and σ_{ob} = 2.5 m s^{-1}. The estimated horizontal decorrelation length scales are L = 43 km for $C_s(r)$, L_{rot} = 39 km for $C_{rot}(r)$ and L_{div} = 53 km for $C_{div}(r)$. Here, C_{rot} and C_{div} denote the error covariance functions for the rotational and divergent parts, respectively, of the background vector wind field, while $C_s(r) = C_{rot}(r) + C_{div}(r)$ is the resolvable-scale part of $C_+(r)$ [see (4.4)-(4.5) of XW]. The rotational and divergent wind error variances are estimated, respectively, by $C_{rot}(0) = \sigma_{rot}^2$ = 77 m^2 s^{-2} and $C_{div}(0) = \sigma_{div}^2$ = 63 m^2 s^{-2}. The associated error standard deviations (σ_{rot} = 8.8 m s^{-1} and σ_{div} = 7.9 m s^{-1}) are quite large. The reason could be due to the fact that the predicted squall line is dislocated to the north of the observed one (by 30-40 km) and so are the associated low-level horizontal shear and convergence along the predicted squall line in the background wind filed.

As r decreases into the range of $r < r_o$ (= 2 km), the normalized innovation covariances (shown by + signs in Fig. 2a) start to increase rapidly (can be seen from a enlarged Fig. 2a but not shown here), indicating that the observation errors are correlated between neighborhood gates within the range of $r < r_o$. The difference between the + signs and the fitted (green) curve within the range of $0 \leq r < r_o$ in Fig. 2a reveals the gross structure of the observation error covariance (C_{ll}^{ob}).

5. Radar data assimilation

The previously developed three-and-half-dimensional variational (3.5dVar) method (Xu et al. 2001a; Gu et al. 2001, referred to as GGX) is upgraded and used in this section to assimilate the phased array radar data into the COAMPS runs for the squall line case mentioned in section 2. In each data assimilation cycle, the 3.5dVar assimilates three consecutive radar volume scans to produce incremental vector velocity fields on two time levels (between the three volume scans) and then uses the analyzed vector velocity fields to produce incremental analyses of perturbation pressure and potential temperature at the middle time level. The first (or second) incremental vector velocity field is produced at the middle time level between the first and second (or second and third) volume scans by minimizing the following cost function:

$$J = J_{bk} + J_{ob} + J_{ms} + J_{rm}, \quad (3)$$

where the four terms on the right-hand side are weak-form constraints imposed, respectively, by the observations (from the two volume scans but treated as at the middle time level), by the mass continuity equation (formulated at the middle time level), by the radial-momentum equation (formulated at the middle time level with the radial-velocity time tendency term computed from the two volume scans), and by the background field (at the middle time level).

In the upgraded 3.5dVar, the first three terms have the same forms as those in GGX except but the weight for J_{ob} is determined not purely empirically but based on the observation error estimated in section 4. In the previous 3.5dVar, J_{bk} was formulated simply with a scalar weight [see (2) of GGX] that ignored the background error correlation. In the upgraded 3.5dVar, the background term is formulated by

$$\begin{aligned} J_{\mathrm{bk}} &= |\mathbf{B}_1^{-1/2}\boldsymbol{\psi}|^2 + |\mathbf{B}_2^{-1/2}\boldsymbol{\chi}|^2 + |\mathbf{B}_3^{-1/2}\mathbf{w}|^2 \\ &= |\boldsymbol{\Psi}|^2 + |\mathbf{X}|^2 + |\mathbf{W}|^2. \end{aligned} \tag{4}$$

Here $\mathbf{B}_1$, $\mathbf{B}_2$ and $\mathbf{B}_3$ denote the error covariance matrices for the background streamfunction, velocity potential and vertical velocity, respectively, while $\boldsymbol{\psi}$, $\boldsymbol{\chi}$ and $\mathbf{w}$ denote the state vectors of the grid fields of the incremental streamfunction, velocity potential and vertical velocity, respectively. In (4), the incremental vector velocity is converted to ($\boldsymbol{\psi}$, $\boldsymbol{\chi}$, $\mathbf{w}$) and then to ($\boldsymbol{\Psi}$, $\mathbf{X}$, $\mathbf{W}$). Each horizontal grid field of ($\boldsymbol{\Psi}$, $\mathbf{X}$, $\mathbf{W}$) is expressed by an expansion of quadratic B-spline basis functions on coarse finite-element meshes (Xu et al. 2001b), so the final control variables are the B-spline coefficients of ($\boldsymbol{\Psi}$, $\mathbf{X}$, $\mathbf{W}$). The recursive filter (Purser et al. 2003) is used to mimic the background covariance matrices and transform ($\boldsymbol{\Psi}$, $\mathbf{X}$, $\mathbf{W}$) back to ($\boldsymbol{\psi}$, $\boldsymbol{\chi}$, $\mathbf{w}$).

From the estimated background vector wind error power spectra (not shown) in section 4, one can estimate the streamfunction and velocity potential error covariance functions [see (2.8) of XW]. However, as these covariance functions are approximated by Gaussian functions in the recursive filter, the variances and horizontal decorrelation length scales can be estimated by $\sigma_\psi{}^2 = \sigma_{\mathrm{rot}}{}^2 L_{\mathrm{rot}}{}^2$ and $L_\psi = \sqrt{2} L_{\mathrm{rot}}$, respectively, for the streamfunction, and by $\sigma_\chi{}^2 = \sigma_{\mathrm{div}}{}^2 L_{\mathrm{div}}{}^2$ and $L_\chi = \sqrt{2} L_{\mathrm{div}}$, respectively, for the velocity potential. Here, we simply set $\sigma_{\mathrm{rot}} = \sigma_{\mathrm{div}} = \sigma = 8.4$ m s^{-1} and $L_{\mathrm{rot}} = L_{\mathrm{div}} = L = 6\Delta x = 42$ km based on those estimated in section 4. By using the mass continuity equation, the error variance and horizontal decorrelation length scale for the vertical velocity can be estimated by $\sigma_w{}^2 = 2\sigma_{\mathrm{div}}{}^2 D_w{}^2 / L_{\mathrm{div}}{}^2$ and $L_w = (\sqrt{2}/\sqrt{3}) L_{\mathrm{div}}$. Here, D_w is the vertical decorrelation length scale for the vertical velocity and is set to $D_w = \Delta z$ (vertical grid spacing). The vertical decorrelation length scales for the streamfunction and velocity potential are set to $D_\psi = D_w$ and $D_\chi = D_w/\sqrt{3}$, respectively. The above parameter values are used with the recursive filter to model the three error covariance matrices in (4). By using the standard conjugate gradient algorithm, the costfunction J in (3) is minimized efficiently in the space spanned by the B-spline coefficients of ($\boldsymbol{\Psi}$, $\mathbf{X}$, $\mathbf{W}$). The estimated B-spline coefficients are then transformed back to ($\boldsymbol{\psi}$, $\boldsymbol{\chi}$, $\mathbf{w}$) and finally to the incremental vector velocity and added to the background velocity on the COAMPS grid.

Once the vector velocity fields are updated at the aforementioned two time levels (between the three volume scans in each assimilation cycle), they are used to produce incremental analyses of perturbation pressure and potential temperature. These analyses minimize the same cost functions as in GGX except that the background terms are reformulated by replacing the original scalar weights with their respective inverse background error covariance matrices. Again, the error covariance functions are approximated by Gaussian functions. The recursive filter and B-spline expansions are used to facilitate the computation in the same way as described for the background term in (4). The horizontal and vertical decorrelation length scales are set to $L_p = L_\psi$ and $D_p = D_\psi$ respectively, for the perturbation pressure, and to $L_\theta = L_p$ and $D_\theta = D_p/\sqrt{3}$, respectively, for the perturbation potential temperature.

After the perturbation pressure and potential temperature fields are updated by the above incremental analyses, the model predicted water vapor mixing ratio q_{v} is adjusted based on the reflectivity difference obtained by subtracting the model predicted positive-only (in dBZ) reflectivity from the radar observed positive-only (in dBZ) reflectivity (interpolated onto the model grid). If the difference is larger than 10 dBZ and the vertical velocity is non-negative (or negative), then q_{v} is adjusted to the saturated value (or 80% of the saturated value). This adjustment is similar to that in GGX except that it is based on the reflectivity difference instead of radar observed reflectivity. Furthermore, if the reflectivity difference is negative and below -5 dBZ, then q_{v} is adjusted to the value interpolated in x- and y-directions from the nearest grid points where the reflectivity difference $\geq$ -5 dBZ. This negative adjustment is new in the upgraded 3.5dVar and is found to be effective in removing model incorrectly predicted reflectivity (and associated clouds and precipitation). The improvement is especially significant in the reflectivity predictions as indicated by our comparison experiments with and without the negative q_{v} adjustment (not shown).

By using the upgraded 3.5dVar, the first three volume scans of the quality-controlled phased array data are assimilated through a single cycle from 2108 to 2112 UTC, and then a test forecast run, called test-1, is launched. Another test run, called test-3, is performed by assimilating the first nine volume scans in three cycles from 2108 to 2120 UTC. The reflectivity fields (at 2200 UTC) predicted by the control run, test-1 run and test-3 run are plotted at z = 3.1 km in Figs. 4a, 4b and 4c, respectively. Verified against the (phased array and KTLX) radar observed reflectivity (not shown), the reflectivity field predicted by the test-1 run is more accurate than predicted by the control run but not as accurate as that predicted by the test-3 run.

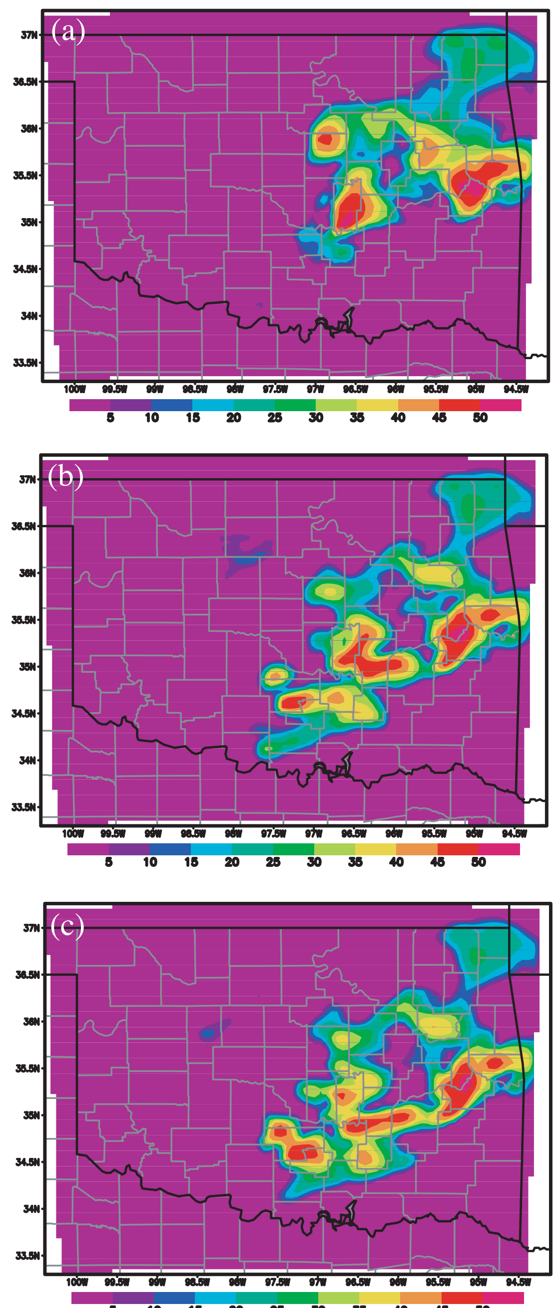

Fig. 4. Predicted reflectivity fields at 2200 UTC and z = 3 km by the control run (a), test-1 run (b) and test-3 run (c).

The model-produced (analyzed and predicted) radial-velocity and reflectivity fields are interpolated to the phased array radar observation points and compared with their respective observed values. The rms differences between the model-produced and observed radial-velocity fields are plotted as functions of time in Fig. 5. As shown, the rms difference is reduced by the analysis in each assimilation cycle although the reductions produced by the analyses in the second and third assimilation cycles are relatively small and their impacts last only about 30 minutes. The spatial correlation coefficients between the model-produced and observed reflectivity fields are plotted in Fig. 6. As shown, the correlation is enhanced by the analysis in each assimilation cycle and the impact produced by each analysis can last a relatively long time (several hours).

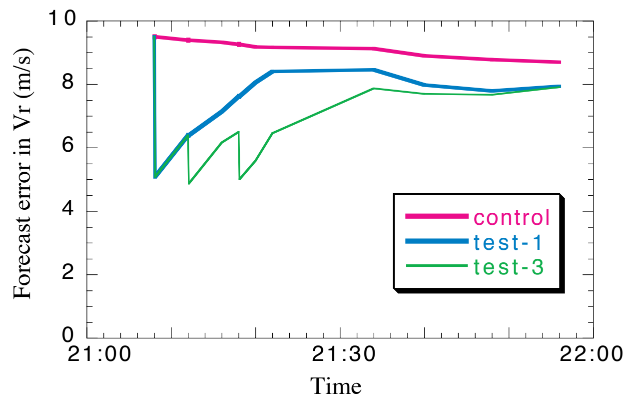

Fig. 5. The rms differences between the model-produced and observed radial-velocity fields (averaged in the observation space). The red, blue and green curves are for the results obtained from the control run, test-1 run and test-3 run, respectively.

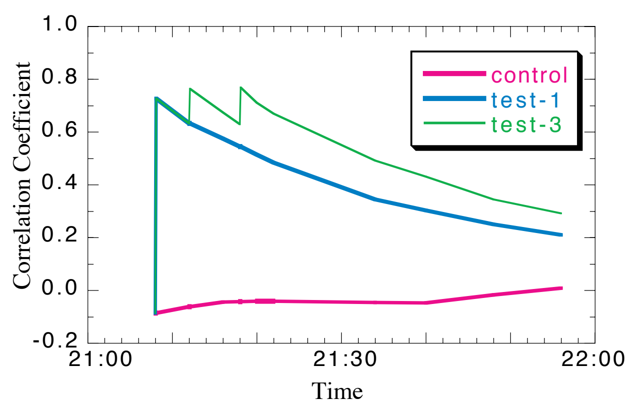

Fig. 6. As in Fig. 5 but for the spatial correlation coefficients between the model-produced and observed reflectivity fields in the observation space.

6. Summary

An initial effort has been made in assimilating phased array radar data and the goal is to improve numerical analyses and predictions of severe storms. To achieve this goal, a comprehensive approach is being taken to attack problems in three important aspects: (i) phased array radar data quality control to meet the high-quality standard required by data assimilation, (ii) estimation of phased array radar radial-velocity observation error variance and background wind error covariance, and (iii) phased array radar data assimilation using the estimated error statistics. This approach is demonstrated in this paper for a squall line case. The results show that using the COAMPS background can simplify the three-step dealiasing although the phased array radar data used in this paper appear to be noisier than the KTLX data (for the same squall line case). With the fast phased array radar scans, radial-velocity innovation data can be accumulated rapidly, so the unknown radar radial-velocity observation error variance and background wind error covariance can be estimated nearly real-time by using the statistical method and thinning strategy developed in this paper. The estimated error variance and covariance can be used by the 3.5dVar (upgraded in this paper) with the COAMPS to improve the numerical analyses and predictions of the squall line.

Acknowledgments. The authors are thankful to Kurt Hondl, Richard Adams and Douglas Forsyth for their help in obtaining the phased array radar data. The research work was supported by the NOAA High Performance Computing and Communications (HPCC) program, by the FAA contract IA# DTFA03-01-X-9007 to NSSL, and by the ONR Grants N000140310822 and N000140410312 to the University of Oklahoma.

References

Forsyth, D. E., J. F. Kimpel, D. S. Zrnic, R. Ferek, J. F. Heimmer, T. J. McNellis, J. E. Crain, A. M. Shapiro, R. J. Vogt, and W. Benner, 2005: The national weather radar testbed (Phased-Array). *32nd Conference on Radar Meteorology*, 24-29 October 2005, Albuquerque, New Mexico, Amer. Meteor. Soc., 12R.3.

Gong, J., L. Wang, and Q. Xu, 2003: A three-step dealiasing method for Doppler velocity data quality control. *J. Atmos. & Oceanic Technology*, **20**, 1738-1748.

Gu, W., H. Gu, and Q. Xu, 2001: Impact of single-Doppler radar observations on numerical prediction of 7 May 1995 Oklahoma squall line. *Fifth Symposium on Integrated Observing Systems*, 14-19 January 2001, Albuquerque, New Mexico, Amer. Meteor. Soc., 139–142.

Hodur, R. M., 1997: The Naval Research Laboratory's coupled ocean/atmosphere mesoscale prediction system (COAMPS). *Mon. Wea. Rev*., **125**, 1414-1430.

Kessler, E., 1969: *On the distribution and continuity of water substance in atmospheric circulation. Meteor. Monogr.*, **10**, No. 32, Amer. Meteor. Soc., 84 pp.

Purser, R. J., and W.-S Wu, D. F. Parrish, and N. M. Roberts, 2003a: Numerical aspects of the application of recursive filters to variational statistical analysis. Part I: Spatially homogeneous and isotropic Gaussian covariances. *Mon. Wea. Rev*., **131**, 1524--1535.

Xu, Q., and J. Gong, 2003: Background error covariance functions for Doppler radial-wind analysis. *Quart. J. Roy. Meteor. Soc.*, **129**, 1703-1720.

Xu, Q., H. Gu and W. Gu, 2001a: A variational method for Doppler radar data assimilation. Preprints, *Fifth Symposium on Integrated Observing Systems*, 14-19 January 2001, Albuquerque, New Mexico, Amer. Meteor. Soc., 118–121.

Xu, Q., H. Gu, and S. Yang, 2001b: Simple adjoint method for three-dimensional wind retrievals from single-Doppler radar. *Quart. J. Roy. Meteor. Soc.*, **127**, 1053-1067.

Xu, Q., L. Wang, and K. Nai, 2003: Error covariance estimation for Doppler wind data assimilation. Preprints, *31th Conference on Radar Meteorology*, 6–12 August 2003, Seattle, Washington, Amer. Meteor. Soc., 108-109.

Xu, Q., and L. Wei, 2001: Estimation of three-dimensional error covariances. Part II: Analysis of wind innovation vectors. *Mon. Wea. Rev*., **129**, 2939-2954.